STRUCTURAL BIOLOGY

Molecular mechanism of the ischemia-induced regulatory switch in mammalian complex I

Daniel N. Grba†, John J. Wright†, Zhan Yin‡, William Fisher, Judy Hirst*

Respiratory complex I is an efficient driver for oxidative phosphorylation in mammalian mitochondria, but its uncontrolled catalysis under challenging conditions leads to oxidative stress and cellular damage. Ischemic conditions switch complex I from rapid, reversible catalysis into a dormant state that protects upon reoxygenation, but the molecular basis for the switch is unknown. We combined precise biochemical definition of complex I catalysis with high-resolution cryo–electron microscopy structures in the phospholipid bilayer of coupled vesicles to reveal the mechanism of the transition into the dormant state, modulated by membrane interactions. By implementing a versatile membrane system to unite structure and function, attributing catalytic and regulatory properties to specific structural states, we define how a conformational switch in complex I controls its physiological roles.

R espiratory complex I (1–3), one of the largest membrane-bound enzymes in mammalian cells, powers adenosine triphosphate (ATP) synthesis in mitochondria. Under physiologically favorable conditions, complex I (NADH:ubiquinone oxidoreductase) captures the free energy from electron transfer from NADH (reduced nicotinamide adenine dinucleotide) to ubiquinone to drive protons across the mitochondrial inner membrane in an efficient energy converting reaction. However, when forward catalysis is blocked, the same efficient mechanisms run in reverse or along different routes, leading to reactive oxygen species production and cellular damage (4, 5). Regulatory mechanisms that switch the enzyme off under unfavorable conditions therefore protect the cell (6–8). During ischemia, when lack of oxygen prevents catalysis, the "deactive transition" converts complex I to a dormant state (9–11), minimizing oxidative damage when oxygen returns during reperfusion and catalysis resumes. Mammalian complex I therefore exists in different catalytic and regulatory states, either on or off the catalytic cycle, depending on the mitochondrial conditions. Single-particle cryo–electron microscopy (cryo-EM) (12, 13) has revolutionized our ability to determine high-resolution structures of complex I and its homologs from multiple species and to isolate multiple distinct states from heterogeneous mixtures (14–26). However, structures observed for complex I in different states, without accompanying biochemical, biophysical, or physiological data to support their assignments, have been interpreted as both catalytic and regulatory spe-

cies, creating a wide variety of contradictory models (14–16, 19, 20, 27) and leaving fundamental questions unanswered. To develop our understanding of complex I further, it is crucial to integrate structural and functional information into a single coherent and robust picture.

In this work, we present high-resolution structures of mammalian (*Bos taurus*, bovine) complex I, isolated from ischemic heart tissue and then embedded into phospholipid vesicle membranes containing ubiquinone-10 (Fig. 1). In these complex I–containing proteoliposomes (CI-PLs), the enzyme can be characterized in detail and switched between different regulatory states to investigate the transitions. The catalytic capability of the CI-PLs can be demonstrated by adding a partner ubiquinol-10 oxidase (the alternative oxidase, AOX) to enable rapid and reversible catalysis (28) with rates that match the maximum rates observed in native membranes (Fig. 2A) (29). By using different combinations of partner enzymes, the system can be set to catalyze NADH-driven ATP synthesis or NAD⁺ reduction by reverse electron transfer (RET), both mediated by a substantial proton-motive force (30, 31). In this work, we combined biochemical, biophysical, and cryo-EM data on CI-PLs (fig. S1) to identify the structural states that occur in the deactive transition of mammalian complex I, underpinning its role in ischemia-reperfusion injury (5–8), and to determine the mechanisms of the transitions between them. Through the reconstitution of highly active CI into CI-PLs suitable for cryo-EM, comprehensive biochemical definition of the enzyme states present, and advanced application of single-particle cryo-EM methods, we establish a quality threshold for structure-focused studies of complex I catalysis and regulation.

Closed and open states in the membrane

Cryo-EM images of CI in CI-PLs, flash frozen onto graphene oxide grids, were collected and

separated into distinct populations (Fig. 1). The first classification separated CI molecules embedded in the membrane with their large hydrophilic domain, which extends into the mitochondrial matrix in vivo, facing either out of the PL lumen (CI-out) or into the PL lumen (CI-in) (Fig. 1, A and B). The proportion of CI-out is ~65%, determined by both cryo-EM classification encompassing the surrounding bilayer and by biochemical assays that rely on accessibility of the NADH-binding site (CI-out only versus CI-total when the membrane is permeabilized) (Fig. 2B). In both orientations, density for the surrounding bilayer is clearly visible, curving away from the protein membrane domain (Fig. 1A) and allowing visualization of the complex in a typical 50-nm-diameter proteoliposome (Fig. 1B). The second classification separated both CI-out and CI-in into two major conformational states, which we refer to as the "closed" and "open" states (14) (Fig. 1C). Further classifications indicated that the closed conformation is structurally homogenous but separated the open state into two similar but distinct states termed open1 and open2. The three states (closed, open1, and open2) are related by rotation of the hydrophilic domain and "heel" relative to the rest of the membrane domain (fig. S2, A to C). This rotation is apparent visually as the opening and closing of the angle between the domains, changing the secondary domain interface between subunits NDUFA10 (membrane domain) and NDUFA5 (hydrophilic domain) (fig. S2D) (14, 32, 33). The highest quality map (CI-out-closed), refined to 2.5-Å resolution, and near-complete protein models were built to all six maps together with ordered phospholipids and water molecules (Fig. 1D, figs. S3 to S6, and tables S1 and S2). The maps and models show how amphipathic helices at the base of the hydrophilic domain that anchor the complex to the membrane interface influence the membrane topology and how the packing of transmembrane helices (TMHs) in the membrane domain adjusts the complex to the curvature (fig. S7). Otherwise, the maps and models for outward- and inward-facing states are essentially identical.

The homogenous closed structures determined in CI-PLs match well to equivalent closed structures determined previously in *n*-dodecyl β-D-maltoside (DDM) detergent micelles and phospholipid nanodiscs (17, 32) but with the observation of a new interdomain contact mediated by supernumerary subunit NDUFAB1 and a Zn²⁺ bound to the mitochondrially encoded subunit ND4 (fig. S8). However, the open structures differ markedly. The open1 (most closed-like open) state has not been observed previously, and open2 is shifted toward the closed end of the "open spectrum" relative to the open state in DDM or nanodiscs. Having previously observed DDM molecules bound behind the ND5 C-terminal transverse helix

Medical Research Council Mitochondrial Biology Unit, University of Cambridge, Keith Peters Building, Cambridge Biomedical Campus, Hills Road, Cambridge CB2 0XY, UK.
*Corresponding author. Email: jh480@cam.ac.uk
†These authors contributed equally to this work.
‡Present address: Department of Biochemistry, University of Cambridge, Tennis Court Road, Cambridge CB2 1GA, UK.
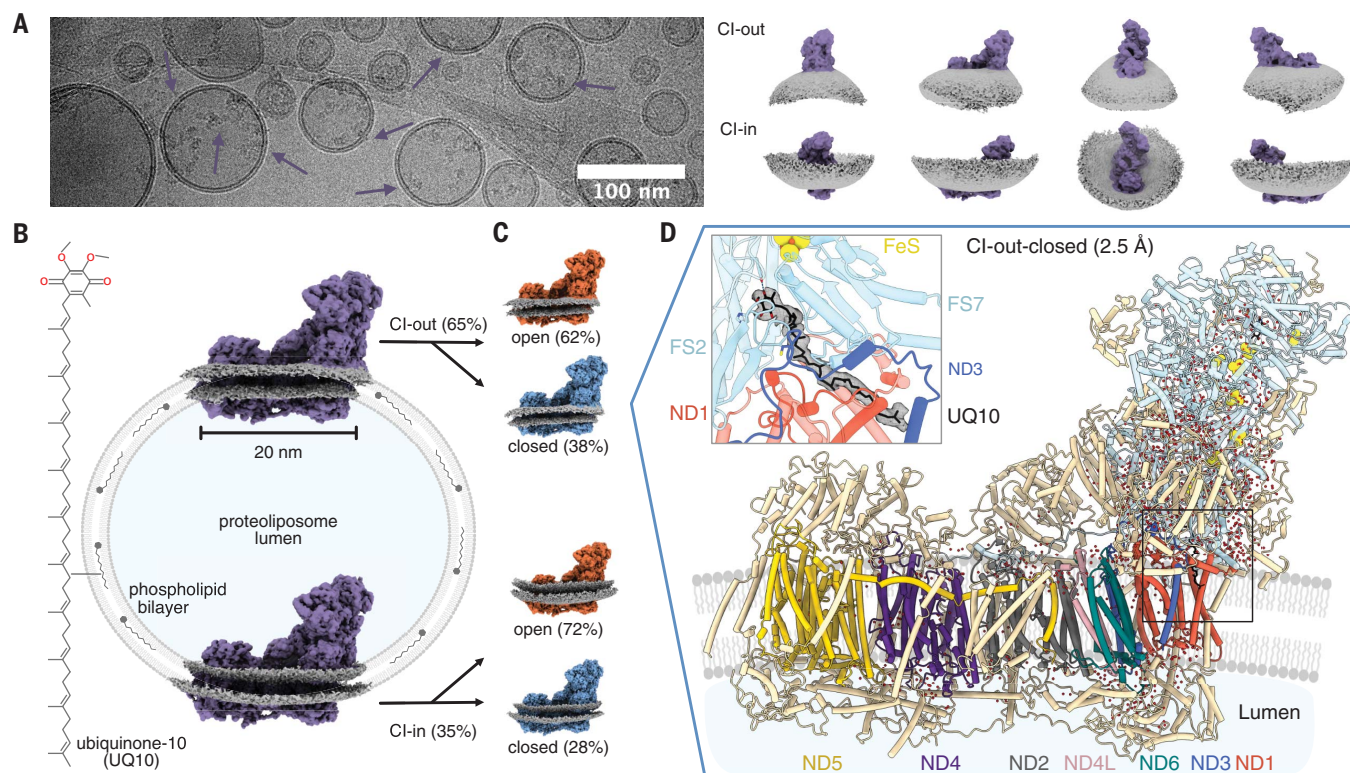
Fig. 1. Generation of high-resolution structures for complex I in proteoliposomes. (**A**) An example micrograph (CI in CI-PLs marked with arrows) and three-dimensional volumes for CI embedded in CI-PLs facing outwards (CI-out) and inwards (CI-in). (**B**) Visualization of CI reconstituted into CI-PLs containing ubiquinone-10. The cryo-EM density for the lipid bilayer (gray) around the enzyme (purple) was clipped and extrapolated to display a typical 50-nm-diameter liposome. (**C**) CI-out and CI-in were classified into open (orange) and closed (blue) states and processed to generate high-resolution maps. (**D**) The model for CI-out-closed (2.5-Å resolution) is shown with water molecules (spheres) and ubiquinone-10 in the substrate-binding site (inset). Conserved core subunits are in light blue (hydrophilic domain) or labeled in color (membrane domain), and supernumerary subunits are in beige.

(*25*) and inserted into the narrow ubiquinone binding channel in the open state in nanodiscs (*17*), we have here switched the detergent used for purification to lauryl maltose neopentyl glycol (LMNG), which is equivalent to two DDM molecules joined together and expected to be too bulky to enter the channel (*15*). No detergent molecules are observed in any of our structures in proteoliposomes (fig. S6). However, the extreme-open "slack" state observed previously in DDM and nanodiscs (*17, 32*), which exhibits substantial disorder and disruption in key regions, including subunit NDUFA11 and the C terminus of ND5, and is also expected to be catalytically inactive (*17, 34*), is absent from our CI-PLs formed from LMNG-purified CI but present in an equivalent preparation of CI-PLs formed from DDM-purified CI (DDM-CI-PLs) (figs. S9 to S11 and table S3). Otherwise, the closed and open structures from the two detergents match well, showing the influence of the stabilizing PL membrane environment. We conclude that the slack state is a DDM-induced artifact. The importance of considering detergent effects was also highlighted in cryo-EM analyses of complex I from the yeast *Chaetomium thermo-*

philum and the bacteria *Escherichia coli*, in which purification in DDM or LMNG altered the distributions of states observed (*20, 21*). In the first part of our analysis, open1 and open2, which are shown below to be biochemically indistinguishable, will be treated as a single open state.

Assigning functions to structural states

Two competing models currently assign the closed and open states observed by cryo-EM in samples of mammalian CI, which have all been isolated from ischemic tissue, to different frameworks. The first postulates that they are an ensemble of resting states (*32, 33, 35, 36*) caught undergoing the deactive transition, which began when oxygen was depleted and catalysis stopped (*9–11*). The second postulates that they are an ensemble of catalytic intermediates (*14, 20*) caught at different points on the catalytic cycle when turnover stopped. Further progress on understanding the mechanism and regulation of CI requires the correct model to be confirmed. The biochemical characteristics of the states involved in the deactive transition have long been established (*9–11*). The active ready-to-go resting state can imme-

diately begin forward (NADH:ubiquinone oxidoreduction) or reverse (RET) catalysis upon introduction of substrates so it displays linear (constant rate) steady-state NADH oxidation. The active state is also insensitive to thiol-reactive reagents that derivatize $Cys39^{ND3}$ on the $TMH1-2^{ND3}$ loop adjacent to the ubiquinone-binding site (*37, 38*). By contrast, the deactive dormant resting state requires substrate-induced reactivation to catalyze in the forward direction, exhibiting an initial catalytic "lag phase" during its reactivation, and is unable to start catalyzing in reverse (*9, 31*), a feature that is considered protective against oxidative damage during reperfusion (*8, 39*). In the deactive state, $Cys39^{ND3}$ is sensitive to derivatization, which prevents reactivation by locking the enzyme in an inactive state (*37, 38*). The active state deactivates slowly and spontaneously at physiological temperatures (~38°C in bovine heart) in the absence of substrates for turnover (*9*).

In our "as-prepared" CI-PLs containing CI isolated directly from ischemic heart tissue, cryo-EM classification determined that 35% of the molecules are closed (65% are open), with a slightly higher proportion closed in the outward-facing population (Figs. 1C and 2C).

Fig. 2. Biochemical properties of complex I in CI-PLs. (**A**) Maximal rates of NADH oxidation in as-prepared (AP) and deactivated (D) cryo-EM samples of CI-PLs measured with the ubiquinol oxidase AOX in the assay buffer ($n = 3$, ± SD). Gramicidin A (GramA; to dissipate the proton-motive force, 0.5 μg mL^{-1}) and piericidin A (PierA; to inhibit CI, 1 μM) were added as indicated. An indicative value for CI in mitochondrial membranes is provided for comparison, calculated on the basis that 10% of the protein present is CI (29). (**B**) Proportion of CI-out in cryo-EM samples determined by using the NADH: APAD$^+$ oxidoreduction assay ($n = 3$, ± SD) and from the cryoEM particle distribution. (**C**) The proportion of closed-state complex I in AP-CI-PLs and D-CI-PLs determined by using the sensitivity of the rate of NADH:O$_2$ oxidoreduction to NEM (assay; $n = 3$, ± S.D.) by cryo-EM particle classification and by mass spectrometry (MS) following isotopic IAM labeling ($n = 3$, ± SD). MS data are from three independent CI-PL reconstitutions. The inset figure presents the values from the cryo-EM data for AP-CI-PLs to match the CI-out and CI-total populations determined by biochemical assays and MS, respectively. (**D**) The lag phase observed in complex I activity assays is due to the presence of open states ($n = 3$, ± SD). A mixture of closed and open states in an as-prepared sample of CI-PLs was (i) treated with DTNB (only the closed population catalyzes, displaying linear catalysis), (ii) deactivated (the previously closed population opens and catalyzes with a lag phase), then (iii) labeled with NEM (both populations are inactive). Each sample was then treated with DTT to remove the DTNB. In (i), both states catalyze, and the mixture displays a lag phase; in (ii), the whole population is open, and the lag phase is increased; and in (iii), only the open population catalyzes with a lag phase. See fig. S12G for a matching experiment with only IAM.
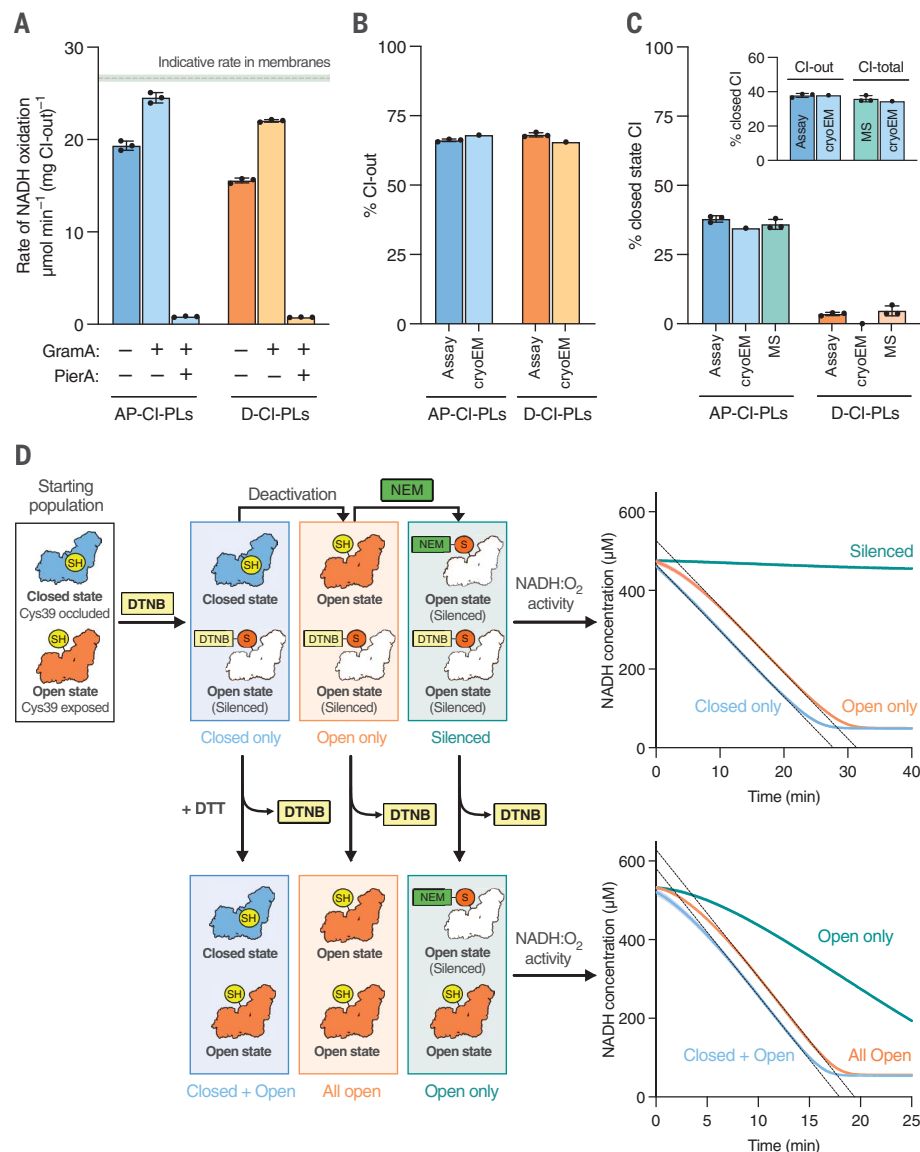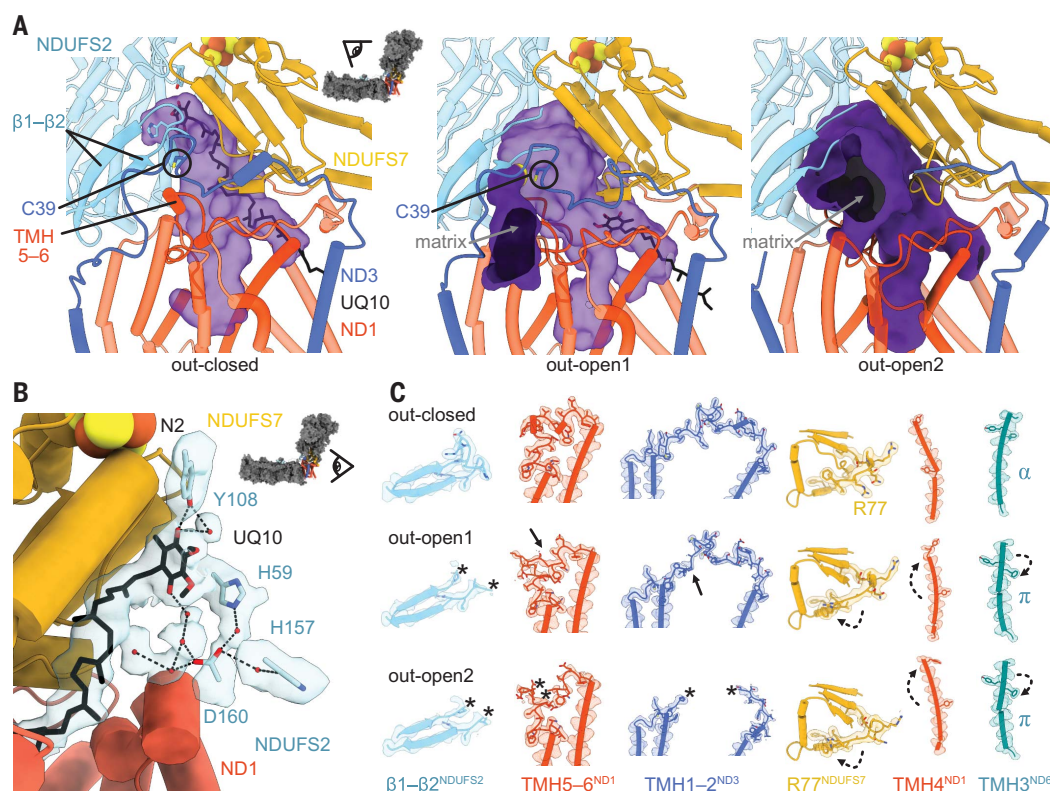
The cryo-EM values were compared with data from three biochemical analyses for the active and deactive states. Firstly, we used two methods that rely on Cys39^{ND3} only being accessible in the deactive state (*31, 38*). In a standard approach, we treated the CI-PLs with a thiol-reactive reagent and used activity assays (which report only on CI-out, as only its NADH-binding site is accessible) to determine the proportion of inactivated enzyme. Three thiol-reactive reagents—*N*-ethyl maleimide (NEM), iodoacetamide (IAM), and 5,5′-dithiobis-(2-nitrobenzoic acid) (DTNB)—all gave similar results (fig. S12A). We also used a sequence of isotopic labeling and mass spectrometry to measure total (CI-out and CI-in combined) Cys39^{ND3} labeling directly (*40*) (fig. S13). In both cases, the biochemical active/deactive proportions were equal to the cryo-EM closed/open proportions (Fig. 2C), consistent with

structure models that show Cys39^{ND3} occluded in the closed state but exposed and solvent accessible in open states (Fig. 3A) (*14, 32, 33, 35, 41*). Secondly, we tested for the catalytic lag phase that is a well-established deactive feature by using alkaline conditions to prolong reactivation (*9, 10, 37*). We used DTNB to derivatize Cys39^{ND3} reversibly [the DTNB label can be removed with the disulfide-reducing agent dithiothreitol (DTT)] (fig. S12B) (*42*) and a standard thermal deactivation of CI-PLs (37°C for 20 min without substrates) (fig. S12C) to deactivate all the enzyme (*31, 35*). The deactivation treatment in vitro replicates the effects on CI of an extended period of tissue ischemia in vivo. The catalytic lag phase was only observed when substrates were supplied to the (underivatized) open enzyme, and catalysis was linear with no lag phase when only the closed enzyme was able to catalyze (Fig. 2D).

Deactivated CI-PLs (D-CI-PLs) show all the deactive biochemical characteristics, including full recovery of their catalytic activity following reactivation, and derivatization of Cys39^{ND3} determined by activity assays and mass spectrometry analyses (Fig. 2, A to C, and fig. S12, B to D). In cryo-EM analyses of D-CI-PLs, all the CI molecules were in the open state (figs. S14 to S17 and table S4). The open1 and open2 structures determined in D-CI-PLs were indistinguishable from those determined in as-prepared CI-PLs (fig. S18), so the deactive enzyme generated by simulating ischemia in vitro is identical to that present (at lower levels) in as-prepared samples from ischemic tissue. Our results demonstrate that the cryo-EM closed state is the ready-to-go active resting state, the cryo-EM open states are the dormant, deactive resting states, and the distribution of states in as-prepared samples of CI from

Fig. 3. Local features of complex I structures in CI-PLs. (**A**) The ubiquinone-10 (UQ10)–binding channel in the closed, open1, and open2 states. Closed: The UQ10-binding channel (purple, semitransparent surface) is sealed from the matrix, UQ10 is fully inserted, and Cys39[ND3] is buried from the matrix. Open1: The UQ10-binding channel is sealed from the matrix, UQ10 is partly inserted, and Cys39[ND3] is exposed to the matrix (purple, solid surface, with yellow indicating the contribution from Cys39[ND3]). Open2: The UQ10-binding channel is exposed to the matrix (purple, solid surface), no bound UQ10 is present, and Cys39[ND3] is exposed to the matrix. (**B**) The bound UQ10 in the CI-out-closed state reveals two hydrogen-bonding networks of water molecules (red spheres) that complete its connection to the proposed ligands (His59[NDUFS2] and Tyr108[NDUFS2]) for protonation upon reduction by the terminal iron-sulfur cluster, N2. The semitransparent surface shows the cryo-EM density (2-Å distance, threshold value 0.03). (**C**) The local elements that correlate with closed and open structural states: β1-β2[NDUFS2] loop (ordered in closed and progressively less ordered in open1 and open2), TMH5-6[ND1] loop (ordered in closed with short α-helical features, ordered in open1 but with helical definition lost, and minor disorder in open2), TMH2-3[ND3] loop (ordered in closed, ordered and shifted in open1, and disordered in open2), Arg77[NDUFS7], TMH3[ND6] α helix or π bulge, and TMH4[ND1]. Cryo-EM density is shown (at thresholds 0.1, 0.1, 0.09, 0.1, 0.1, and 0.09; left to right), with residues of interest shown as sticks. Solid and dashed arrows indicate localized disorder and movement, respectively, relative to the closed state. Asterisks indicate peptides not observed because of disordering. See also fig. S20 and table S5. Single-letter abbreviations for the amino acid residues referenced in this figure are as follows: R, Arg; D, Asp; C, Cys; Y, Tyr; H, His.

ischemic tissue (*43*) represents a snapshot of the resting enzyme undergoing the deactive transition in the absence of substrates.

The ubiquinone-10 binding site

Our CI-closed structures exhibit well-ordered density for ubiquinone-10, inserted fully into its active site with one of the ubiquinone carbonyls directly hydrogen bonded to Tyr108[NDUFS2], a proposed ligand and proton donor for ubiquinone reduction (*44, 45*) (Fig. 3B). Focused classifications were unable to separate any substates, suggesting that the site is saturated by a single ubiquinone-10 binding pose, consistent with free equilibration with the ~10-mM ubiquinone-10 in the PL bilayer [relative to Michaelis constant (K_m) values of 0.5 to 1.5 mM for catalyzing CI-PLs] (*30, 31, 46*). Earlier deep-bound ubiquinone-10 structures, determined in either nanodiscs or detergent micelles, have exhibited lower occupancy levels and have either been in a pre-reactive conformation lacking direct interaction with Tyr108[NDUFS2] (*17*) or without sufficient resolution to model water molecules (*19*). Here, waters are observed around the ubiquinone headgroup in a single hydrogen-bonding network that indirectly connects both proposed proton donors (His59[NDUFS2] and Tyr108[NDUFS2]) to both ubiquinone carbonyls (Fig. 3B). Otherwise, the local, detailed features (top, Fig. 3C and table S5) and discrete networks of residues and water molecules in the glutamate-rich region known as the E-channel and the hydrophilic axis (fig. S19) match previous closed-state mammalian structures (*17, 25*). The tightly structured, closed ubiquinone-binding site at the interface between the hydrophilic and membrane domains likely determines this consistency.

In as-prepared and deactivated CI-PLs, the open state was resolved into two states, open1 and open2, which differ in the status of loops at the ubiquinone-binding site and domain interface, but otherwise display all the established structural hallmarks of open, deactive states (Fig. 3C and table S5) (*36*). In the hitherto-unknown open1 state, the TMH1-2[ND3] loop is ordered in a closed-like conformation. At the deepest part of the ubiquinone-binding channel, the β1-β2[NDUFS2] loop is disordered, and the trigonal interaction (*22, 25*) between Cys39[ND3], His55[NDUFS2], and Tyr127[ND1] has been lost. Notably, although Cys39[ND3] is solvent accessible and available for derivatization by thiol-labeling reagents, the ubiquinone-binding

channel is sealed from the matrix (Fig. 3A and fig. S20). Open1 thereby combines an open global conformation with a closed ubiquinone-binding site, breaking the previously described (*14*) correlation between the two features. Ubiquinone-10 is partially inserted into the lower section of the open1 channel, and the TMH5-6[ND1] loop is ordered in a closed-like conformation. By contrast, in the open2 state, both the TMH1-2[ND3] and β1-β2[NDUFS2] loops are disordered (Cys39[ND3] remains accessible), and the ubiquinone binding channel is open to the matrix (Fig. 3A). Although only a poorly defined density hinting at ubiquinone-10 is observed, the TMH5-6[ND1] loop remains in its closed-like conformation, albeit with increased disorder at residues 208 and 209. Local disorder is also observed nearby in the TMH3-4[ND6] loop (residues 79 to 85) and NDUFA9 C-terminal domain (residues 325 to 332). The ordered status of the TMH5-6[ND1] loop in both open1 and open2 in CI-PLs (and conserved in DDM-CI-PLs) is in striking contrast to the extended disorder observed previously in open states in detergent micelles and nanodiscs (*14, 17, 32, 33, 35, 36*) (table S5). The presence of two distinct open states in CI-PLs raises

the question of whether they are both canonically deactive: Both states are sensitive to thiol-derivatizing reagents (fig. S20), but because we cannot control their formation independently, we cannot confirm whether both or just one cause the open state–dependent catalytic lag phase. Therefore, we exploited the fact that deactive CI is unable to catalyze RET and assessed the ability of our CI-PLs to catalyze RET in a coreconstituted system (31) that uses F_1F_O ATP synthase (ATPase) to create a proton-motive force (fig. S21). As-prepared CI-ATPase-PLs exhibited 35% of the maximum RET rate (achieved following a prereaction activation step), which matches the proportion found in the closed state by the NEM assay. Furthermore, no RET could be observed for deactivated CI-ATPase-PLs, which contain only the open1 and open2 states. Although we cannot exclude that the proton-motive force and/or reduction of the ubiquinone pool for RET change the balance between open1 and open2 or even promote the closure of open1, these results suggest strongly that open1 and open2 are both deactive states.

Structural basis for deactivation

The spontaneous but slow nature of the deactive transition indicates that deactivation is an exergonic process with a high activation energy, but how the structural changes that occur define the energy landscape for the transition and confer these properties is not understood. In this work, we show how the membrane environment influences the stabilities of the states and the transition between them. Comparing the membrane-bound closed and open states, the hydrophilic domain rotates about an axis projected on subunit ND1 through the membrane domain (Fig. 4A and fig. S2, A and B), with ND1 and surrounding supernumerary subunits as a pivot point. $TMH2-8^{ND1}$, supported underneath by NDUFA8, NDUFA1, and NDUFA13, bend on closing or extend on opening (Fig. 4, A and B). The long, curved NDUFA13 helix bends or extends alongside, whereas NDUFA8 and NDUFA1 are fixed and appear to brace the pivoting of NDUFA13 at its helix-breaking Pro-72 residue. We propose that $TMH2-8^{ND1}$ extending and straightening provide the primary driving force for deactivation, with their bending and deformation back into closed, catalytically active states demanding energization. Opposing the straightening of these loaded helical "springs," interaction of the amphipathic NDUFA9 C-terminal domain with the lipid bilayer creates a counterbalance (Fig. 4C). In the closed state, an abundance of well-ordered NDUFA9-associated lipids embed and anchor it to the bilayer, whereas, in open states, rotation of the hydrophilic domain lifts NDUFA9 away from the bilayer. On the opposite side of the domain, amphipathic helices on NDUFS8 and NDUFA12 are pushed into
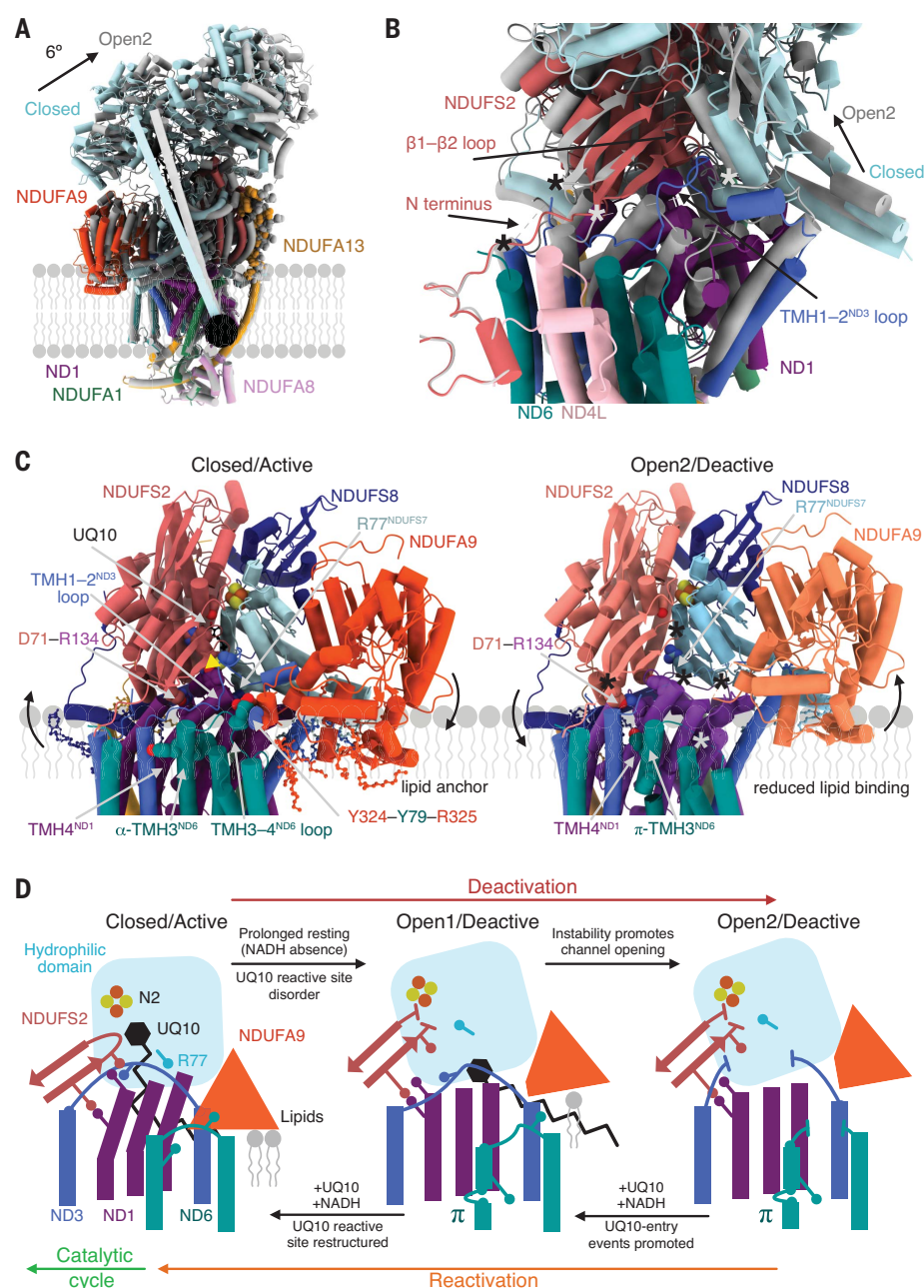
Fig. 4. Structural transition between the closed (active) and open (deactive) resting states. (**A**) Global comparison of the closed (active) (color) and open2 (deactive) (gray) structures superpositioned on their membrane domains showing relevant supernumerary subunits from behind the interface between the hydrophilic and membrane domains. The axis of rotation is marked as a black circle, with the rotation (6°) planes shown. The N terminus of NDUFA13 extends up the hydrophilic domain and is shown as spheres. (**B**) The same alignment as in (A) viewed from the front and focused on the interface between the hydrophilic and membrane domains to show the movement of the ND1 TMHs relative to ND6 and the rotation of the hydrophilic domain. Asterisks indicate disorder in the open2 (deactive) model, in which coordinated colors link the missing residues. (**C**) The same superpositioned models as in (B), with only subunits of interest labeled, and the closed or active and open2 (deactive) states shown side by side. Lipids and UQ10 are shown in ball-and-stick representation, and iron-sulfur cluster N2 and key residues are shown as spheres. The residues of the trigonal junction are indicated by the yellow triangle. Asterisks indicate regions of loop disorder. (**D**) Schematic overview of the structural elements involved in the deactivation and reactivation transitions between the closed (active) and open2 (deactive) states corresponding to (C). Circles on sticks indicate stabilizing residue interactions, such as the trigonal junction of His55^{NDUFS2}, Tyr127^{ND1}, and Cys39^{ND3}; Arg77^{NDUFS7} and the ion pair Arg134^{ND1}-Asp71^{NDUFS2}; and the packing interactions Tyr324^{NDUFA9}-Tyr79^{ND6}-Arg325^{NDUFA9} and Phe68$^{TMH3-ND6}$ with ND1. See also movie S1.

the bilayer in open states, creating an intrinsic stabilizing "buoyancy." Amphipathic helices in the hydrophilic-domain core subunits likely perform the same role in enzymes, such as *E. coli* complex I, which lack both NDUFA9 and the biochemical characteristics of mammalian-type active-deactive transitions, although they may adopt less altered resting states. Additional protein interactions stabilizing the mammalian closed state (*47*) include the greater buried NDUFA5-NDUFA10 interface (fig. S2D) and the N terminus of NDUFS2 that runs across the matrix surface of the membrane domain, where it is ordered in the closed state but disordered in open states.

Ubiquinone-10 fully inserted into its binding channel in the closed state stabilizes the $\beta 1$-$\beta 2^{NDUFS2}$ loop that carries the essential His59 (*48*), as well as the closed position of Arg77^{NDUFS7}. Upon deactivation, Arg77^{NDUFS7} moves into the channel, blocking substrate entry. Excluding substrate allows the $\beta 1$-$\beta 2^{NDUFS2}$ loop to escape its closed conformation, encouraging His55^{NDUFS2} to break its trigonal interaction with Cys39^{ND3} and TMH4-Tyr127^{ND1} as the latter straightens (Fig. 4C). Asp71 on the $\beta 1$-$\beta 2^{NDUFS2}$ loop retains its ion-pair interaction with TMH4-Arg134^{ND1} as the straightening ND1-TMHs drive rotation of the hydrophilic domain, generating the matrix-exposed Cys39^{ND3} cavity in open1. Further destabilization of the TMH1-2^{ND3} loop, which crosses the rotation interface, occurs on conversion to open2 (Figs. 3A and 4, B to D). Both straightening of the ND1-TMHs and rotation-induced displacement of NDUFA9 destroy the closed-state packing site for TMH3-Phe68^{ND6} and destabilize interactions between TMH3-4–loop-Tyr79^{ND6} and Tyr324-Arg325^{NDUFA9}, promoting the helical rotation of TMH3^{ND6} that generates the hallmark π bulge of the open states (Figs. 3C and 4, C and D). The π bulge (with unfavorable dihedrals, decreased hydrogen bonding, and decreased packing) has an intrinsic driving force to return to an α-helical conformation, aiding reactivation. Prolonged absence of the deep-bound substrate from the closed state thereby promotes the coordinated, exergonic opening transition of a network of interacting structural elements, which are otherwise finely counterbalanced to maintain the metastable closed states in which catalysis occurs. Returning deactive open states to catalysis is determined by the mitochondrial conditions as it requires energy input from NADH-driven ubiquinone-10 reduction: to refold and reform local elements and drive domain rotation; regenerate the strained, loaded helical springs in ND1; and reanchor NDUFA9 to the lipid bilayer, repoising the system for energy transduction (Fig. 4D).

Discussion

The closed resting state in CI-PLs contains ubiquinone-10 fully loaded into the catalytic site, reflecting its ready-to-go nature. We propose that the open1 and open2 states that form during ischemia are deactive, dormant states that must be reactivated to return to catalysis, with their off-cycle status suggested by their inability to initiate reverse catalysis, the reaction that produces reactive oxidative species during reperfusion. Specifically, the open-state π bulge in ND6-TMH3 disengages the proton-pumping reactions in the membrane arm from the redox machinery (*49*), and energy input from repeated NADH oxidation events is needed to reengage the two. Our assignment of the open conformations to the deactive, dormant states that form during ischemia is not consistent with a competing proposal that they are catalytic intermediates (*14*), which was based on the presence of heterogeneous open states in ovine (*Ovis ares*) complex I (including the artifactual slack state) prepared from ischemic heart tissue. The inability of slack-type states to reactivate (*34*) explains their presence in ice-cold samples of the ovine enzyme in the presence of substrates (*14*), alongside deactive open states that persist owing to their slow and temperature-dependent reactivation. Consistent with our model, the closed state appeared on addition of substrates to all-open preparations of *E. coli* complex I (*20*), and slow closing may explain the delay in proton pumping observed for the *E. coli* enzyme after the onset of redox catalysis (*50*). Our data confirm that purposeful deactivation (under conditions that simulate tissue ischemia) of mammalian CI-PLs merely converts the closed (active) enzyme into the same open (deactive) enzyme already there at lower levels, completing the deactivation process that began in the tissue. Our data are not consistent with the alternate "deactive" structure created by heat-treating the ovine enzyme in detergent micelles and characterized by the tilting of TMH4^{ND6} (*14*), which was presented without substantive biochemical data to confirm its identity or ability to return to catalysis and exhibited considerable structural disorder and alteration reminiscent of the bovine slack state (*17*).

Although cryo-EM analyses provide no evidence that complex I opens and closes during catalysis, the coordinated changes of the deactive transition may provide clues to its catalytic mechanism. The same local elements that change conformation together during deactivation may change individually during catalysis, but in a local and constrained fashion (*51*), without breaking open the ubiquinone-binding site (and thereby incurring the energy costs of desolvation, refolding, and resealing) or globally opening the enzyme. Open1, a globally open state with a sealed ubiquinone-binding site, is between the closed and open2 states on the opening spectrum, and we suggest that it forms first during deactivation, is the dominant open state in vivo, and is an intermediate in reactivation

of open2 formed when substrate entry begins to restructure the channel. Ubiquinone-10 binding is essential for reactivation, but substrate exchange for catalysis occurs within closed-only states. Our model is consistent with observations of quinone partly or fully inserted into the closed channel in mycobacterial complex I (*26*) and with molecular dynamics simulations that have illustrated its transit through the closed channel on physiologically relevant timescales (*52*, *53*). We thus disagree that it is necessary to form open2-like states for solvent-assisted substrate exchange during catalysis (*14*, *20*). The conflicting interpretations of structural data discussed here underline the need for robust functional analyses to be used alongside structural analyses in membrane environments in future mechanistic studies, as enabled by our CI-PLs.

The methods we have developed for structure-focused studies of catalysis and regulation in respiratory complex I offer possibilities for mechanistically challenging systems that require membrane environments for their function and/or suffer from poor cryo-EM particle distribution and orientation biases in their detergent-solubilized forms. Cryo-EM on proteoliposomes has already been demonstrated by Yao and colleagues (*54*), who reported a 3.8-Å resolution structure of the AcrB multidrug-resistant transporter embedded in liposomes on graphene grids. Several ion channels have now also been determined in liposomes and separated into different states (*55*), and a 2.7-Å resolution structure of a high-conductance Ca^{2+}-activated K^+ channel has recently been determined in native membrane vesicles (*56*). In this work, we demonstrate high-resolution structures and discrete states for a nonsymmetrical protein using standard grid preparation methods. The native-like environment and ubiquinone-10 substrate provided in CI-PLs, combined with the exquisite biochemical control that the system allows, has allowed a sophisticated structural evaluation of the resting states of mammalian complex I and their functional and physiological relevance, highlighting options for therapeutic intervention (*6*, *7*). The CI-PLs system now provides opportunities to study the catalytic intermediates that are generated under catalyzing and energy-transducing conditions.

REFERENCES AND NOTES

1. J. Hirst, *Annu. Rev. Biochem.* **82**, 551–575 (2013).
2. K. Fiedorczuk, L. A. Sazanov, *Trends Cell Biol.* **28**, 835–867 (2018).
3. K. Parey, C. Wirth, J. Vonck, V. Zickermann, *Curr. Opin. Struct. Biol.* **63**, 1–9 (2020).
4. M. P. Murphy, *Biochem. J.* **417**, 1–13 (2009).
5. E. T. Chouchani *et al.*, *Cell Metab.* **23**, 254–263 (2016).
6. E. T. Chouchani *et al.*, *Nat. Med.* **19**, 753–759 (2013).
7. A. Galkin, S. Moncada, *Interface Focus* **7**, 20160104 (2017).
8. Z. Yin *et al.*, *Nat. Commun.* **12**, 707 (2021).
9. A. B. Kotlyar, A. D. Vinogradov, *Biochim. Biophys. Acta* **1019**, 151–158 (1990).
10. M. Babot, A. Birch, P. Labarbuta, A. Galkin, *Biochim. Biophys. Acta* **1837**, 1083–1092 (2014).
11. S. Dröse, A. Stepanova, A. Galkin, *Biochim. Biophys. Acta* **1857**, 946–957 (2016).
12. T. Nakane *et al.*, *Nature* **587**, 152–156 (2020).

13. A. Punjani, D. J. Fleet, *J. Struct. Biol.* **213**, 107702 (2021).
14. D. Kampjut, L. A. Sazanov, *Science* **370**, eabc4209 (2020).
15. K. Parey *et al.*, *Sci. Adv.* **7**, eabj3221 (2021).
16. P. Kolata, R. G. Efremov, *eLife* **10**, e68710 (2021).
17. I. Chung *et al.*, *Nat. Commun.* **13**, 2758 (2022).
18. L. Zhou, M. Maldonado, A. Padavannil, F. Guo, J. A. Letts, *Science* **376**, 831–839 (2022).
19. J. Gu, T. Liu, R. Guo, L. Zhang, M. Yang, *Nat. Struct. Mol. Biol.* **29**, 172–182 (2022).
20. V. Kravchuk *et al.*, *Nature* **609**, 808–814 (2022).
21. E. Laube, J. Meier-Credo, J. D. Langer, W. Kühlbrandt, *Sci. Adv.* **8**, eadc9952 (2022).
22. A. A. Agip, I. Chung, A. Sanchez-Martinez, A. J. Whitworth, J. Hirst, *eLife* **12**, e84424 (2023).
23. A. Padavannil, A. Murari, S.-K. Rhooms, E. Owusu-Ansah, J. A. Letts, *eLife* **12**, e84415 (2023).
24. N. Klusch *et al.*, *Nat. Plants* **9**, 142–156 (2023).
25. D. N. Grba, I. Chung, H. R. Bridges, A. A. Agip, J. Hirst, *Sci. Adv.* **9**, eadi1359 (2023).
26. Y. Liang *et al.*, *Proc. Natl. Acad. Sci. U.S.A.* **120**, e2214949120 (2023).
27. H. Kim, P. Saura, M. C. Pöverlein, A. P. Gamiz-Hernandez, V. R. I. Kaila, *J. Am. Chem. Soc.* **145**, 17075–17086 (2023).
28. A. J. Y. Jones *et al.*, *Angew. Chem. Int. Ed.* **55**, 728–731 (2016).
29. K. R. Pryde, J. Hirst, *J. Biol. Chem.* **286**, 18056–18065 (2011).
30. O. Biner, J. G. Fedor, Z. Yin, J. Hirst, *ACS Synth. Biol.* **9**, 1450–1459 (2020).
31. J. J. Wright *et al.*, *J. Am. Chem. Soc.* **144**, 6791–6801 (2022).
32. J. Zhu, K. R. Vinothkumar, J. Hirst, *Nature* **536**, 354–358 (2016).
33. A. A. Agip *et al.*, *Nat. Struct. Mol. Biol.* **25**, 548–556 (2018).
34. A. A. Agip, J. N. Blaza, J. G. Fedor, J. Hirst, *Annu. Rev. Biophys.* **48**, 165–184 (2019).
35. J. N. Blaza, K. R. Vinothkumar, J. Hirst, *Structure* **26**, 312–319. e3 (2018).
36. I. Chung, D. N. Grba, J. J. Wright, J. Hirst, *Curr. Opin. Struct. Biol.* **77**, 102447 (2022).
37. A. B. Kotlyar, V. D. Sled, A. D. Vinogradov, *Biochim. Biophys. Acta* **1098**, 144–150 (1992).
38. A. Galkin *et al.*, *J. Biol. Chem.* **283**, 20907–20913 (2008).
39. E. T. Chouchani *et al.*, *Nature* **515**, 431–435 (2014).
40. N. Burger *et al.*, *Cell Chem. Biol.* **29**, 636–649.e14 (2022).
41. J. A. Letts, K. Fiedorczuk, G. Degliesposti, M. Skehel, L. A. Sazanov, *Mol. Cell* **75**, 1131–1146.e6 (2019).
42. I. S. Gostimskaya, G. Cecchini, A. D. Vinogradov, *Biochim. Biophys. Acta* **1757**, 1155–1161 (2006).
43. N. Gorenkova, E. Robinson, D. J. Grieve, A. Galkin, *Antioxid. Redox Signal.* **19**, 1459–1468 (2013).
44. M. A. Tocilescu *et al.*, *Biochim. Biophys. Acta* **1797**, 625–632 (2010).
45. A. P. Gamiz-Hernandez, A. Jussupow, M. P. Johansson, V. R. I. Kaila, *J. Am. Chem. Soc.* **139**, 16282–16288 (2017).
46. J. G. Fedor, A. J. Y. Jones, A. Di Luca, V. R. I. Kaila, J. Hirst, *Proc. Natl. Acad. Sci. U.S.A.* **114**, 12737–12742 (2017).
47. A. Di Luca, V. R. I. Kaila, *Biochim. Biophys. Acta Bioenerg.* **1862**, 148382 (2021).
48. M. A. Tocilescu, U. Fendel, K. Zwicker, S. Kerscher, U. Brandt, *J. Biol. Chem.* **282**, 29514–29520 (2007).
49. M. Röpke *et al.*, *Proc. Natl. Acad. Sci. U.S.A.* **118**, e2019498118 (2021).
50. N. Belevich, C. von Ballmoos, M. Verkhovskaya, *Biochemistry* **56**, 5691–5697 (2017).
51. A. Cabrera-Orefice *et al.*, *Nat. Commun.* **9**, 4500 (2018).
52. J. Warnau *et al.*, *Proc. Natl. Acad. Sci. U.S.A.* **115**, E8413–E8420 (2018).
53. M. Hoias Teixeira, G. Menegon Arantes, *Biochim. Biophys. Acta Bioenerg.* **1860**, 541–548 (2019).
54. X. Yao, X. Fan, N. Yan, *Proc. Natl. Acad. Sci. U.S.A.* **117**, 18497–18503 (2020).
55. V. S. Mandala, R. MacKinnon, *Proc. Natl. Acad. Sci. U.S.A.* **119**, e2214151119 (2022).
56. X. Tao, C. Zhao, R. MacKinnon, *Proc. Natl. Acad. Sci. U.S.A.* **120**, e2302325120 (2023).

ACKNOWLEDGMENTS

SUPPLEMENTARY MATERIALS